Institute of Faculty of Power and Aeronautical Engineering

Project Report

in the field of study Aerospace Engineering
and specialisation Aerospace Engineering

Comparative Study of Turbulence Models for NACA2412:
uRANS, DES, and LES

Kacper Frelek
student record book number 313668

project supervisor
Msc. Eng. Michał Klamka

WARSAW 2025

Contents

INS/GPS integration, purpose, methods, error analysis.

Abstract.

This study presents a detailed computational investigation of turbulent flow around the NACA 2412 airfoil using three advanced turbulence modeling techniques: Unsteady Reynolds-Averaged Navier-Stokes (uRANS), Detached Eddy Simulation (DES), and Large Eddy Simulation (LES). The primary focus is on evaluating the models' capabilities in predicting and visualizing key flow structures, including pressure, velocity, and vorticity contours. Simulations are performed at a fixed angle of attack and Mach number to ensure consistency and comparability across the models. Emphasis is placed on assessing each model's ability to resolve critical flow features such as boundary layer development, flow separation, and vortex dynamics. Additionally, the computational cost and efficiency of each approach are analyzed. The results provide insights into the trade-offs between accuracy and computational demands, offering guidance for the selection of appropriate turbulence models in high-fidelity aerodynamic analyses. Key findings and visualizations are presented with LaTeX-formatted equations and plots to ensure precision and clarity.

Keywords: NACA 2412, turbulence modeling, uRANS, DES, LES, aerodynamics, CFD

1. Introduction

The accurate prediction of aerodynamic performance and flow behavior around airfoils remains a cornerstone of modern aerospace engineering. Computational Fluid Dynamics (CFD) plays an indispensable role in this field, enabling the detailed analysis of complex flow phenomena. Among the extensively studied airfoil configurations, the NACA 2412 airfoil stands out due to its well-documented aerodynamic properties and widespread application in subsonic and low-speed flight regimes. This airfoil serves as an ideal benchmark for evaluating advanced turbulence modeling techniques.

This project investigates the application of three advanced turbulence models—Unsteady Reynolds-Averaged Navier-Stokes (uRANS), Detached Eddy Simulation (DES), and Large Eddy Simulation (LES)—to the flow around the NACA 2412 airfoil. Each of these models represents a different approach to resolving turbulence, ranging from time-averaged approximations to scale-resolving simulations. The focus of this study is on examining the predictive capabilities of these models in capturing detailed flow structures and complex phenomena, rather than traditional aerodynamic performance metrics such as lift and drag.

The simulations are conducted on the same angle of attack and Reynolds number representative of typical operating conditions. Special emphasis is placed on the visualization and interpretation of flow features using contour plots and other post-processing techniques. By focusing on these aspects, this study aims to provide a deeper understanding of the suitability of uRANS, DES, and LES for resolving detailed flow physics in aerodynamic design and analysis. The insights gained from this investigation will help select the appropriate turbulence models for specific engineering applications.

2. Motivation

Understanding the behavior of turbulent flows around airfoils is critical for the design and optimization of aerodynamic surfaces in aerospace, automotive, and energy industries. The NACA 2412 airfoil, with its wide range of applications and extensive prior research, provides an ideal platform for advancing turbulence modeling techniques. However, accurately capturing the intricate flow structures such as pressure gradients, vorticity, and velocity fields remains a challenge, particularly at higher fidelity levels.

While traditional turbulence models such as RANS offer computational efficiency, their limitations in capturing unsteady flow features and complex separation phenomena necessitate the exploration of more advanced methods like DES and LES. These models promise enhanced accuracy by resolving finer-scale turbulence structures, but they also demand significantly higher computational resources. By conducting a comparative study of uRANS, DES, and LES under identical flow conditions, this project aims to balance accuracy with computational feasibility, providing valuable insights into their applicability for high-fidelity aerodynamic analyses.

This study is motivated by the need to bridge the gap between academic research and practical engineering applications, where selecting the right turbulence model often involves trade-offs between computational cost and the level of detail required. The findings from this work are expected to guide engineers and researchers in making informed decisions when employing CFD tools for complex aerodynamic simulations.

3. Airfoil

The NACA 2412 airfoil was chosen for this study due to its prominence in aerodynamic research and its widespread use in various engineering applications. This airfoil is part of the widely recognized 4-digit series, which is characterized by its straightforward geometric definition and predictable aerodynamic behavior. The NACA 2412, specifically, has a moderate camber and thickness distribution, making it suitable for analyzing flow phenomena in subsonic and low-speed regimes.

This airfoil has been extensively studied in both experimental and computational settings, providing a wealth of reference data for validation and benchmarking. Its popularity in CFD analyses stems from its ability to exhibit critical aerodynamic features such as boundary layer transition, flow separation, and vortex shedding under certain conditions. These characteristics make it an ideal candidate for evaluating turbulence models, as they demand a high level of accuracy in capturing complex flow structures.

By selecting the NACA 2412 (3.1), this project benefits from a well-documented aerodynamic baseline while addressing the challenges of modeling turbulent flows. The insights gained from this study are not only applicable to this specific airfoil but also extend to similar aerodynamic configurations, enhancing the broader understanding of turbulence modeling in CFD.
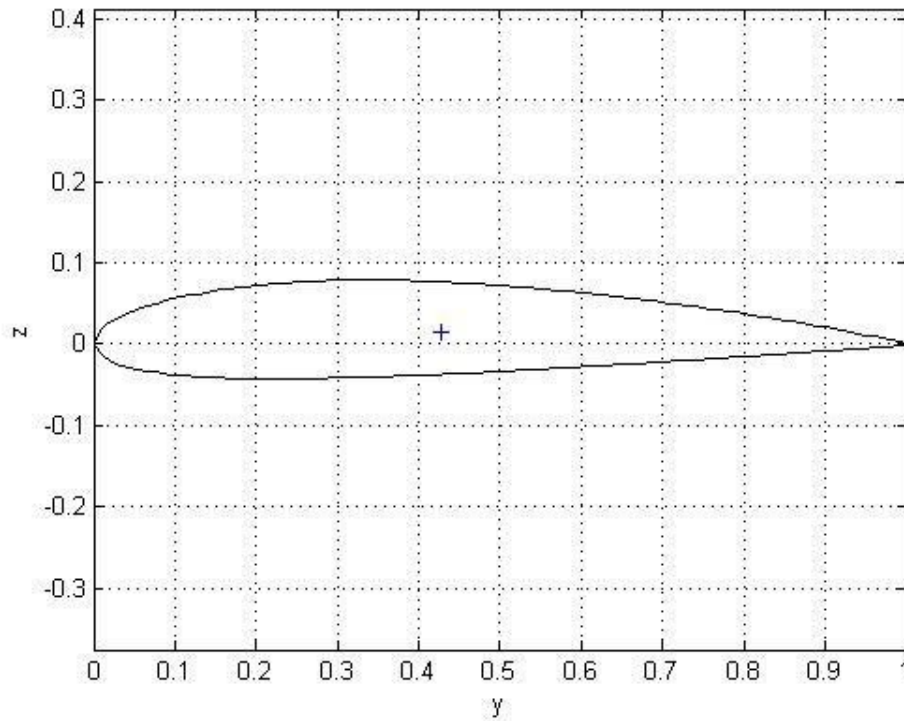

Figure 3.1. Airfoil NACA2412

4. Theoretical Background

4.1. Aerodynamics

4.1.1. Viscosity

In fluid mechanics, all moving bodies interact with a fluid medium, whose properties profoundly influence the motion. Among these properties, viscosity—a measure of a fluid's internal resistance to shear or flow—is one of the most fundamental. Viscosity arises from the transport of molecular momentum and plays a critical role in determining the behavior of fluid flow in various contexts [1].

The study of viscosity is pivotal in understanding fluid mechanics because it influences phenomena such as boundary layer formation, laminar-to-turbulent flow transitions, and drag forces. The viscosity of a fluid is influenced by variables such as temperature, pressure, and flow velocity. Two forms of viscosity are commonly used to characterize fluid behavior: dynamic viscosity (μ) and kinematic viscosity (ν). Dynamic viscosity is defined as the ratio of shear stress to the velocity gradient (Eq. 1), whereas kinematic viscosity represents the ratio of dynamic viscosity to fluid density (Eq. 2).

$$\mu = \frac{\tau}{\frac{du}{dy}} \tag{1}$$

$$\nu = \frac{\mu}{\rho} \tag{2}$$

The effect of viscosity is illustrated through tangential surface shear stress (τ), depicted in Fig. 4.1. Shear stress interacts with pressure (acting normal to the surface), generating a resultant force on a body. This force is resolved into axial (F_x) and vertical (F_y) components, as shown in Eqs. 3 and 4. In the case of an airfoil, these forces significantly influence lift and drag production.

$$F_x = \oint (p\sin\theta + \tau\cos\theta)\,ds \tag{3}$$

$$F_y = \oint (-p\cos\theta + \tau\sin\theta)\,ds \tag{4}$$
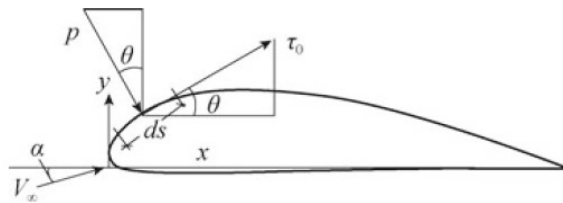

Figure 4.1. Shear stress and pressure acting on an airfoil [2]

4.1.2. Reynolds Number

The Reynolds number (*Re*), introduced by George Stokes in 1851 and later named by Osborne Reynolds in 1908, is a dimensionless parameter that characterizes the nature of fluid flow (Eq. 5). It represents the ratio of inertial forces to viscous forces. A high Reynolds number indicates a dominance of inertial forces, minimizing the influence of viscosity, whereas a low Reynolds number signifies the opposite.

$$Re = \frac{\rho_\infty V_\infty x}{\mu_\infty} = \frac{V_\infty x}{\nu_\infty} \tag{5}$$

Reynolds number plays a key role in determining whether the flow is laminar or turbulent. Understanding this parameter is crucial for predicting aerodynamic performance, especially in airfoil applications, where flow behavior directly impacts lift, drag, and pressure distribution.

4.1.3. Laminar vs. Turbulent Flow

Fluid flows are generally classified as laminar or turbulent, depending on the Reynolds number. In laminar flow, fluid particles move in smooth, orderly layers with minimal mixing, whereas turbulent flow is characterized by chaotic, irregular fluid motion and enhanced mixing [3]. Transition from laminar to turbulent flow occurs at a critical Reynolds number, which depends on specific conditions. For low-speed flows over airfoils, this critical value is approximately $Re \approx 5 \cdot 10^5$ [1].

4.2. Lift, Drag, and Pressure Distribution

The forces of lift and drag are central to aerodynamic performance, and their calculation depends on an accurate understanding of pressure and shear stress distribution over a body. Lift is generated primarily by pressure differences on the upper and lower surfaces of an airfoil, while drag comprises contributions from pressure drag, skin friction drag, and induced drag. The geometry of the airfoil significantly impacts these forces by altering the pressure distribution and flow patterns around it.

An airfoil's shape determines the pressure gradient, which influences boundary layer behavior. A well-designed airfoil minimizes adverse pressure gradients, reducing flow separation and drag while maximizing lift. Additionally, thin airfoils tend to favor laminar flow, reducing drag, while thicker airfoils accommodate higher loads but may increase drag due to earlier transitions to turbulence.

4.3. Mach Regimes

The Mach number (*M*), a dimensionless parameter representing the ratio of an object's speed to the speed of sound in the medium (Eq. 6), categorizes flow regimes into subsonic, transonic, supersonic, and hypersonic. Compressibility effects become significant in flows where $M > 0.3$, altering aerodynamic behavior.

$$M = \frac{u}{c} \tag{6}$$

4.3.1. Compressible vs. Incompressible Flow

While all flows exhibit some degree of compressibility, flows with $M < 0.3$ are typically considered incompressible, as density variations are negligible (Eq. **??**). For higher Mach numbers, compressibility must be accounted for, as it influences lift, drag, and wave propagation phenomena.

$$\frac{\Delta \rho}{\rho} \leq 5 \tag{7}$$

4.4. Boundary Layers and Separation

The boundary layer is a thin region adjacent to a surface where velocity gradients are significant due to the no-slip condition. As shown in Fig. 4.2, boundary layers can be either laminar or turbulent, with properties summarized in Tab. **??**. Laminar boundary layers are thinner with lower friction, while turbulent boundary layers are thicker but better resist flow separation.

Flow separation occurs when the boundary layer detaches from the surface due to an adverse pressure gradient ($\frac{dp}{dx} > 0$). This phenomenon, illustrated in Fig. **??**, results in increased drag and loss of lift, often leading to stall conditions.
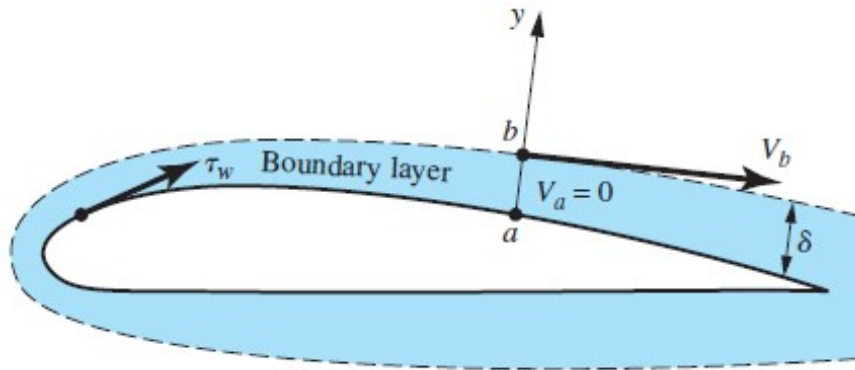

Figure 4.2. Boundary Layer around an airfoil (overemphasized) [1]

5. Basic Principles of Computational Fluid Dynamics

Computational Fluid Dynamics (CFD) is a branch of fluid mechanics that leverages numerical methods and algorithms to solve and analyze problems involving fluid flow, heat transfer, and related physical phenomena. CFD has become an indispensable tool in aerodynamics and aerospace engineering, offering detailed insights into flow behavior that are often unattainable through experimental methods. This section outlines the

foundational principles of CFD, focusing on the governing equations, turbulence modeling approaches, and challenges associated with turbulent flow simulations.

5.1. Governing Equations of Fluid Motion

The motion of fluids is governed by a set of partial differential equations that encapsulate the principles of conservation of mass, momentum, and energy. These are collectively known as the Navier-Stokes equations, which are expressed in their general form as:

- **Continuity Equation:**

$$\frac{\partial \rho}{\partial t} + \nabla \cdot (\rho \mathbf{v}) = 0$$

  This equation ensures the conservation of mass within the fluid domain.

- **Momentum Equation:**

$$\rho \frac{D\mathbf{v}}{Dt} = -\nabla p + \mu \nabla^2 \mathbf{v} + \rho \mathbf{g}$$

  Here, the terms on the right-hand side represent the forces acting on a fluid element, including pressure, viscous, and gravitational forces.

- **Energy Equation:**

$$\frac{\partial}{\partial t}\left(\rho E\right) + \nabla \cdot \left[(\rho E + p)\mathbf{v}\right] = \nabla \cdot (k\nabla T) + \Phi$$

  The energy equation accounts for the conservation of thermal energy, where E is the total energy, T is the temperature, k is the thermal conductivity, and Φ represents viscous dissipation.

These equations are highly nonlinear and coupled, posing significant challenges for direct analytical solutions. Numerical discretization methods are employed to approximate their solutions over a computational grid, making CFD a powerful tool for simulating fluid behavior.

5.2. Turbulence Modeling Approaches

Turbulence is a fundamental yet complex phenomenon characterized by chaotic, unsteady flow structures. Direct Numerical Simulation (DNS) provides the most accurate representation of turbulence by resolving all scales of motion, but its computational expense is prohibitive for most practical applications. Therefore, various turbulence models have been developed to approximate turbulence effects:

- **Reynolds-Averaged Navier-Stokes (RANS):** The RANS approach involves time-averaging the Navier-Stokes equations to filter out turbulence fluctuations. This requires the use of turbulence models such as k-ϵ, k-ω, and Spalart-Allmaras to close the equations.

- **Unsteady Reynolds-Averaged Navier-Stokes (uRANS):** A variant of RANS that incorporates time-dependent averaging, making it suitable for unsteady flows with periodic turbulence.
- **Detached Eddy Simulation (DES):** DES combines RANS modeling in near-wall regions with Large Eddy Simulation (LES) in the outer flow, providing a balance between computational efficiency and accuracy.
- **Large Eddy Simulation (LES):** LES resolves large turbulence structures explicitly while modeling smaller eddies using subgrid-scale models. It offers higher fidelity than RANS but at a significantly greater computational cost.

Model	Time	Cell Size	Accuracy	Applications and Limitations
RANS	Low	$y^+ \approx 1$	Low	Steady flows; poor for separation.
uRANS	Moderate	$y^+ \approx 1$	Moderate	Unsteady flows; limited for large separations.
DES	High	$y^+ < 5, \Delta x \approx \lambda_T$	High	Accurate for separation and wake flows; uses Taylor microscale.
LES	Very High	$\Delta x, \Delta y, \Delta z \approx \eta$	Very High	Resolves turbulence; costly for high Re.

Table 5.1. Comparison of Turbulence Models

The choice of turbulence model depends on the specific flow conditions, computational resources, and desired accuracy. LES and DES are particularly effective for capturing flow separation and wake structures, making them valuable for high-fidelity simulations in aerospace applications.

5.3. Challenges in Simulating Turbulent Flows

Simulating turbulent flows remains one of the most challenging aspects of CFD due to the inherent complexity and multiscale nature of turbulence. Key challenges include:

- **Numerical Discretization:** The accuracy of CFD simulations depends on the choice of spatial and temporal discretization schemes. High-order schemes are often required to reduce numerical diffusion and ensure the accurate capture of flow gradients.
- **Grid Sensitivity:** The quality and resolution of the computational grid significantly impact the results. Finer grids improve accuracy but increase computational cost, necessitating a balance between grid resolution and available resources.
- **Turbulence Modeling Limitations:** While RANS models are computationally efficient, they may fail to capture complex unsteady phenomena such as flow separation

and vortex shedding. LES and DES offer improved accuracy but at a higher computational expense.

- **Boundary Conditions:** Proper implementation of boundary conditions is critical for ensuring the physical validity of simulations. Inadequate boundary conditions can lead to numerical instabilities and inaccuracies.

Addressing these challenges requires careful consideration of the numerical methods, turbulence models, and computational resources. Advances in hardware and algorithms continue to expand the capabilities of CFD, enabling increasingly accurate simulations of turbulent flows in complex geometries.

5.4. Turbulence Models

This section provides a detailed theoretical discussion of the turbulence models employed, their simplifications of the governing equations, specific mesh considerations, and practical implications for simulations in aerodynamics and aerospace applications.

5.4.1. Unsteady Reynolds-Averaged Navier-Stokes (uRANS)

The uRANS approach is based on the Reynolds decomposition of the instantaneous velocity field into mean and fluctuating components:

$$\boldsymbol{u} = \overline{\boldsymbol{u}} + \boldsymbol{u}'$$

Substituting this decomposition into the Navier-Stokes equations and averaging over time yields the Reynolds-Averaged Navier-Stokes (RANS) equations. These equations introduce the Reynolds stress tensor $-\overline{\rho u_i' u_j'}$, representing the influence of turbulent fluctuations on the mean flow. To close the equations, a turbulence model is required.

The SST k-ω model used in this study combines the strengths of the k-ω formulation near walls and the k-ε formulation in free shear flows. The governing equations for the turbulent kinetic energy (k) and the specific dissipation rate (ω) are as follows:

$$\frac{\partial(\rho k)}{\partial t} + \frac{\partial(\rho u_j k)}{\partial x_j} = P_k - \beta^* \rho k \omega + \frac{\partial}{\partial x_j}\left[(\mu + \sigma_k \mu_t)\frac{\partial k}{\partial x_j}\right]$$

$$\frac{\partial(\rho \omega)}{\partial t} + \frac{\partial(\rho u_j \omega)}{\partial x_j} = \alpha \frac{\omega}{k} P_k - \beta \rho \omega^2 + \frac{\partial}{\partial x_j}\left[(\mu + \sigma_\omega \mu_t)\frac{\partial \omega}{\partial x_j}\right]$$

where P_k is the production term, μ_t is the turbulent eddy viscosity, and $\alpha, \beta, \sigma_k, \sigma_\omega$ are empirical constants. The SST formulation blends the equations smoothly across the flow domain, improving accuracy in adverse pressure gradients and separated flows.

For uRANS simulations with the SST k-ω model, the near-wall resolution must satisfy $y^+ \approx 1$ to accurately resolve the viscous sublayer. This typically requires a structured boundary layer mesh with fine spacing in the normal direction to the wall and moderate refinement in regions of expected separation.

uRANS is computationally efficient and suitable for steady or mildly unsteady flows. However, its reliance on modeling all turbulence scales limits its ability to capture large-scale unsteadiness, vortex shedding, and separation-driven flows accurately.

5.4.2. Detached Eddy Simulation (DES)

DES is a hybrid approach that combines the RANS model near walls and LES in regions of separated turbulence. The DES formulation introduces a modified turbulence length scale (L_t), defined as:

$$L_t = \min\left(C_{DES}\Delta, \frac{k^{1/2}}{\omega}\right)$$

where $\Delta = \max(\Delta x, \Delta y, \Delta z)$ is the local grid spacing and C_{DES} is a model constant. This switching criterion ensures that DES behaves as RANS in the boundary layer and transitions to LES in separated and wake regions.

DES requires a near-wall resolution of $y^+ < 5$ for the RANS region and grid spacing in the separated regions on the order of the Taylor microscale (λ_T), defined as:

$$\lambda_T = \sqrt{\frac{\nu\epsilon}{u'}}$$

where ν is the kinematic viscosity, ϵ is the turbulence dissipation rate, and u' is the velocity fluctuation magnitude. Coarser grids in separated regions may cause the model to revert to RANS-like behavior, reducing accuracy.

DES provides a good compromise between accuracy and computational cost, especially for separation-dominated flows and wake turbulence. However, it is sensitive to grid anisotropy and can suffer from the "modeled stress depletion" issue if the grid is not appropriately refined.

5.4.3. Large Eddy Simulation (LES)

LES explicitly resolves large-scale turbulent eddies while modeling the subgrid-scale (SGS) motions using a SGS stress model. The filtered Navier-Stokes equations are the foundation of LES:

$$\frac{\partial \overline{u_i}}{\partial t} + \frac{\partial(\overline{u_i u_j})}{\partial x_j} = -\frac{1}{\rho}\frac{\partial \overline{p}}{\partial x_i} + \nu\frac{\partial^2 \overline{u_i}}{\partial x_j^2} - \frac{\partial \tau_{ij}}{\partial x_j}$$

where $\tau_{ij} = \overline{u_i u_j} - \overline{u_i}\,\overline{u_j}$ is the subgrid-scale stress tensor. The Smagorinsky model is widely used for τ_{ij}, where the eddy viscosity is proportional to the square of the strain rate tensor.

LES demands similar mesh requirements as DES mesh.

LES offers unparalleled accuracy in capturing large-scale turbulence, vortex dynamics, and transient flow features. However, it is computationally intensive, particularly for wall-resolved simulations in high-Reynolds-number flows, and requires high-quality meshes with minimal numerical dissipation.

6. Methodology

6.1. Geometry and Computational Domain

The NACA 2412 airfoil, a widely studied and benchmarked aerodynamic profile, was selected for the analysis. For consistency and to simplify comparisons across different turbulence models, the airfoil was scaled to have a chord length of 1m. The computational domain was carefully designed to minimize boundary interference effects and ensure accurate simulation results.

The computational domain (6.1) was constructed as a denser region surrounding the airfoil, with the following boundary distances relative to the airfoil:

- The pressure far-field boundary was placed 10 m from the airfoil leading edge in radial directions to ensure proper dissipation of aerodynamic disturbances.
- The top and bottom walls of the domain were located 10m from the airfoil chord plane, providing ample spacing to reduce any interference with flow recirculation and wake development.
- The rear boundary of the domain, designed to accommodate wake formation and dissipation, was extended 15 m downstream of the trailing edge.
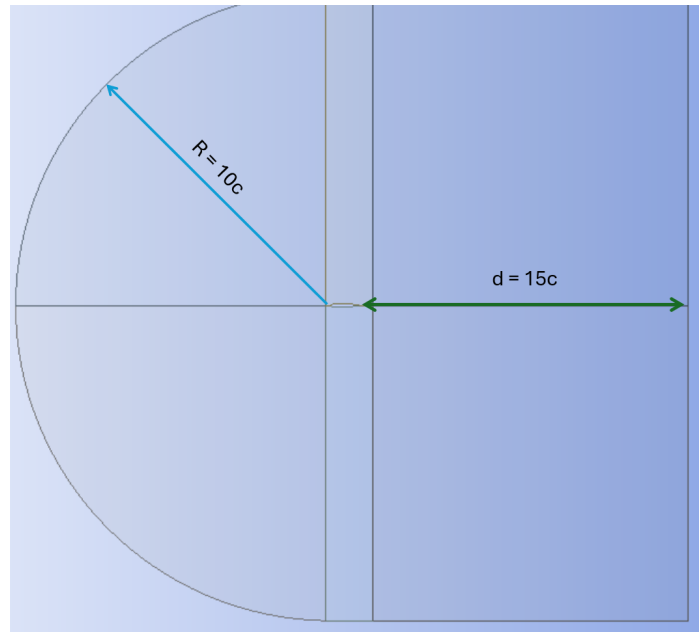
Figure 6.1. Computational domain used for the CFD analysis

This domain configuration, derived from established guidelines in computational aerodynamics, ensures that the simulated flow field captures the relevant physics while avoiding reflections or artificial constraints that could compromise the accuracy of the results.

6.2. Meshing Strategy

A tailored meshing strategy was implemented for each turbulence model to address their distinct requirements for spatial resolution while optimizing computational efficiency. High-quality unstructured meshes were generated using advanced meshing tools, ensuring accurate resolution of key flow features, particularly in regions of interest such as the boundary layer and wake. Specific meshing considerations for each turbulence model are summarized below:

- **uRANS (SST k-ω):** An unstructured mesh (6.4) with dense boundary layer (6.5) refinement was employed to achieve $y^+ \approx 1$ (6.2), ensuring resolution of the viscous sublayer. The boundary layer region consisted of 13 inflation layers with a growth rate of 1.2. Outside the boundary layer, the mesh was coarsened (6.3) to reduce computational costs without compromising accuracy in resolving mean flow structures.
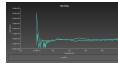
Figure 6.2. y+ values over an airfoil
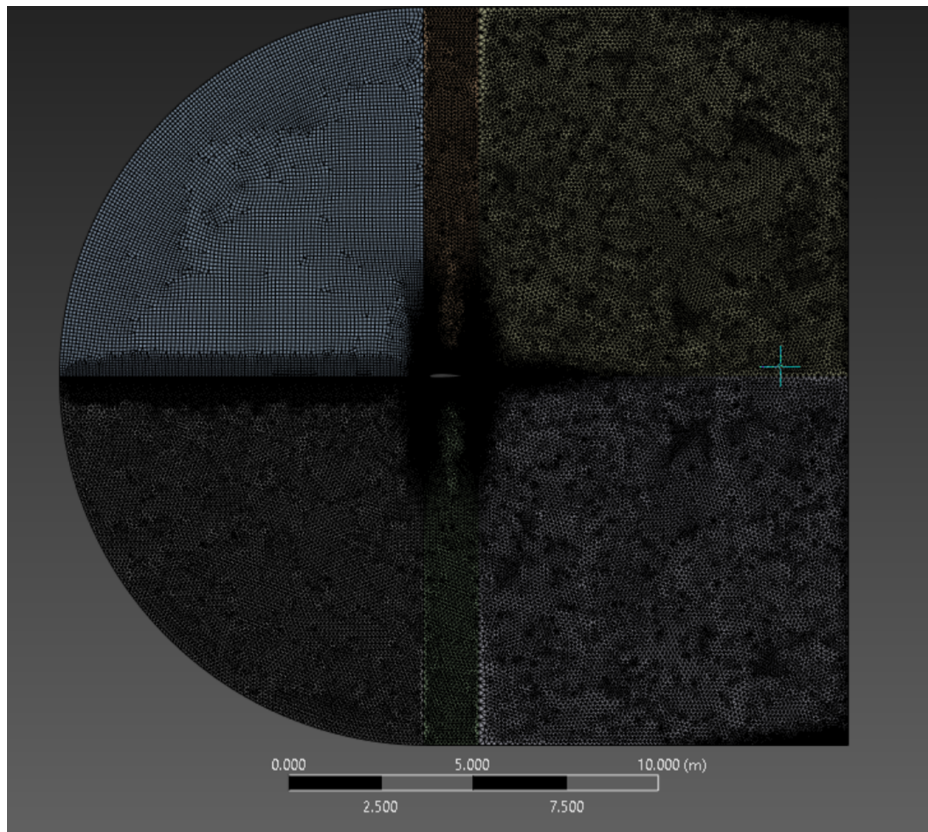
Figure 6.3. Overview look for a uRANS mesh
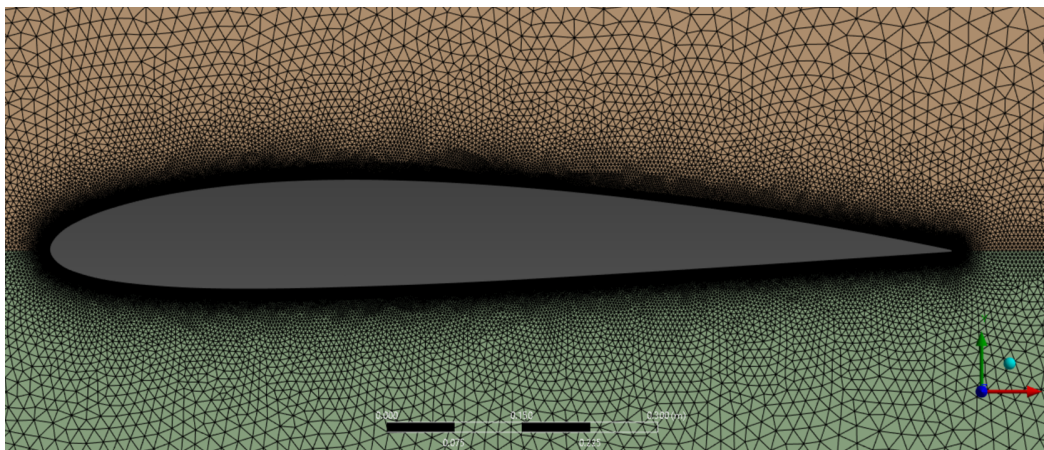
Figure 6.4. Closeup look for a uRANS mesh
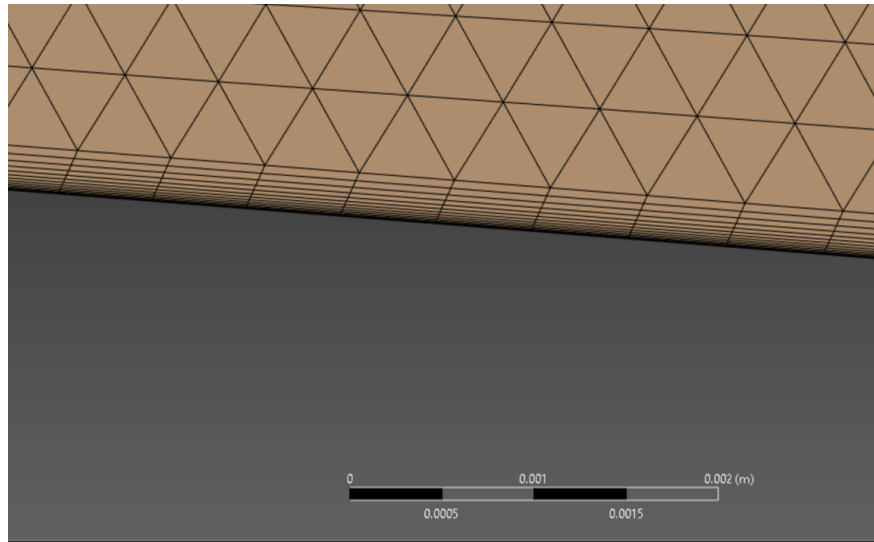
Figure 6.5. Inflation layers close up of a uRANS mesh

- **DES:** A hybrid unstructured mesh was used for DES (6.6). Near-wall regions featured a fine structured mesh (6.8) to maintain $y^+ < 5$, while the separated flow regions and wake were resolved with an unstructured grid (6.7). The wake mesh was designed to approach the Taylor microscale λ_T, facilitating accurate resolution of the transition between RANS and LES regions.
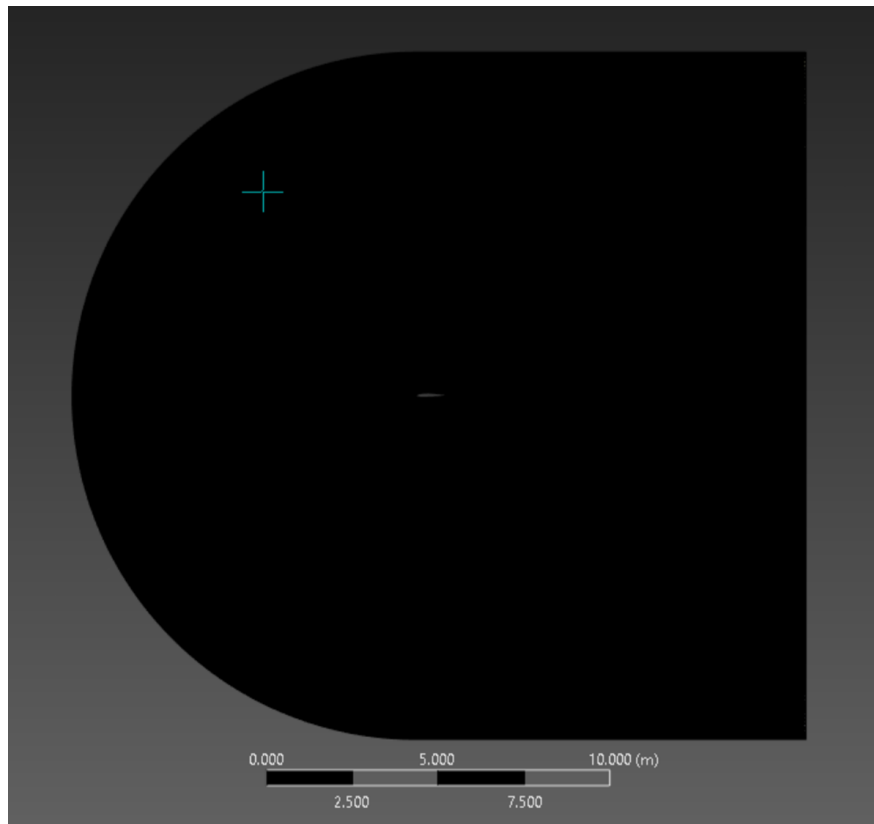
Figure 6.6. Overview look for a DES mesh
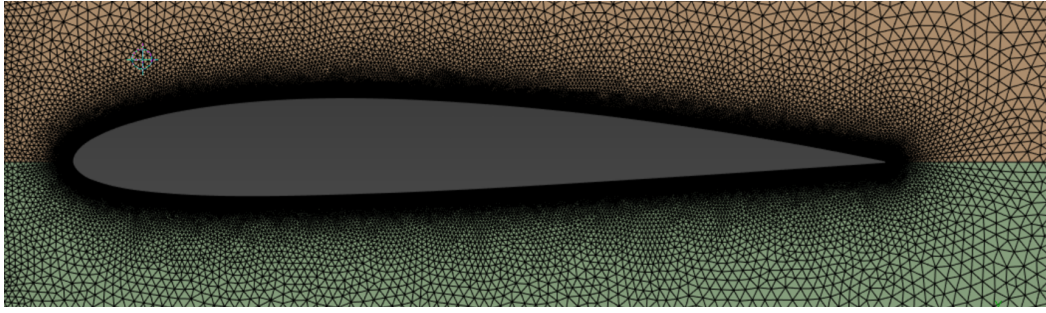
Figure 6.7. Closeup look for a DES mesh
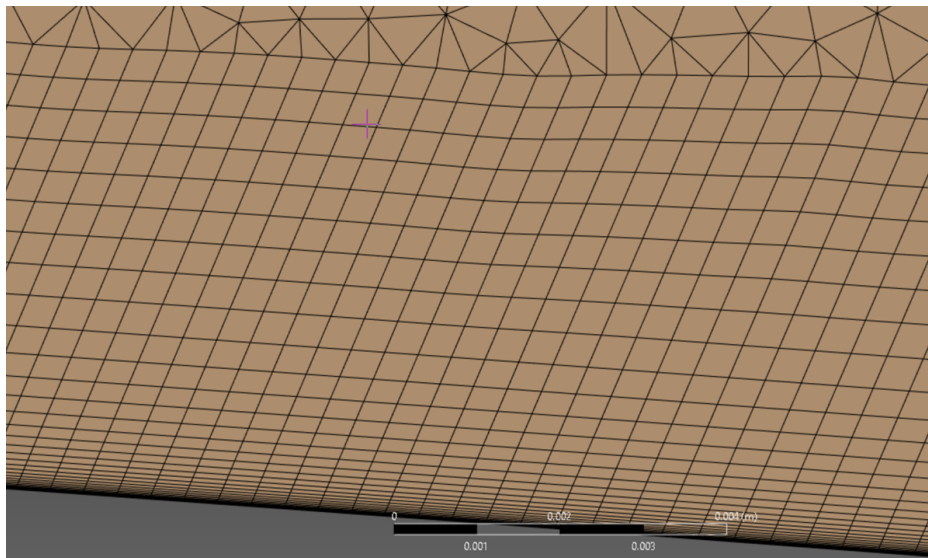
Figure 6.8. Inflation layers close up of a DES mesh

- **LES:** For LES simulations, an unstructured mesh was applied throughout the domain (6.9), with further refinement in the wake and separated regions (6.10) to approach the Kolmogorov scale η. The boundary layer resolution was enhanced using finer inflation layers (6.11) to capture near-wall turbulence structures effectively, meeting the strict requirements of wall-resolved LES.
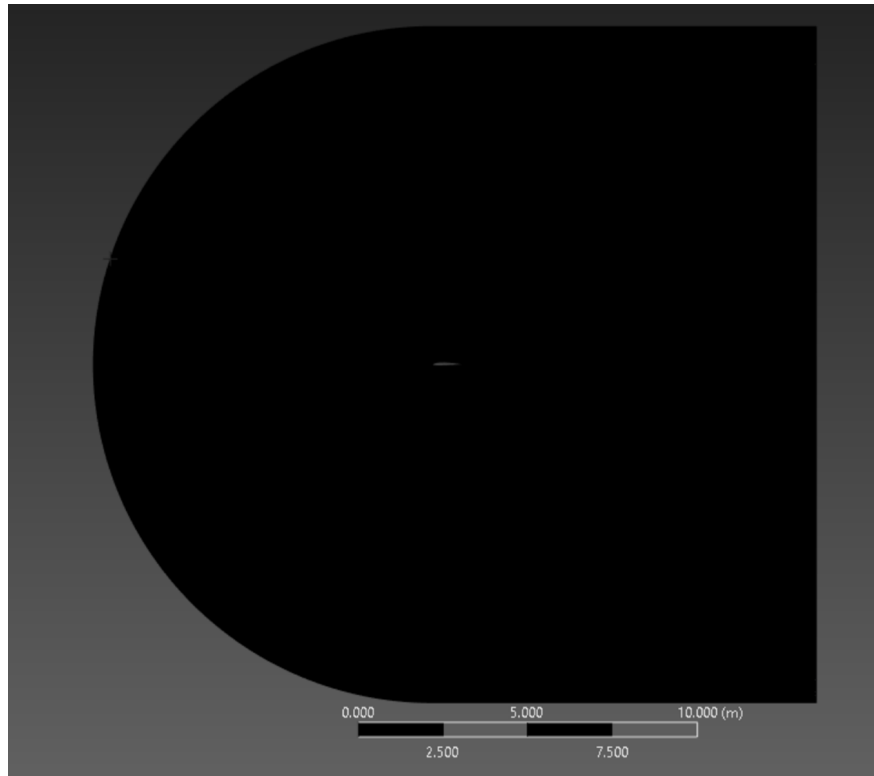
Figure 6.9. Overview look for a LES mesh
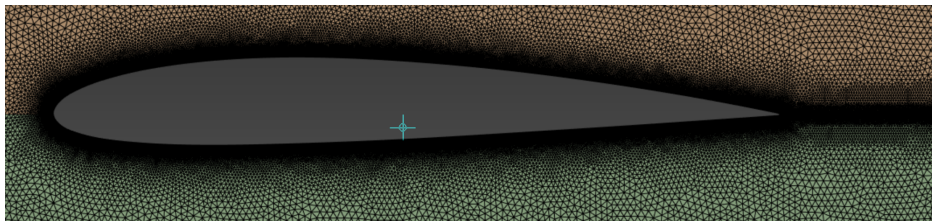
Figure 6.10. Closeup look for a LES mesh
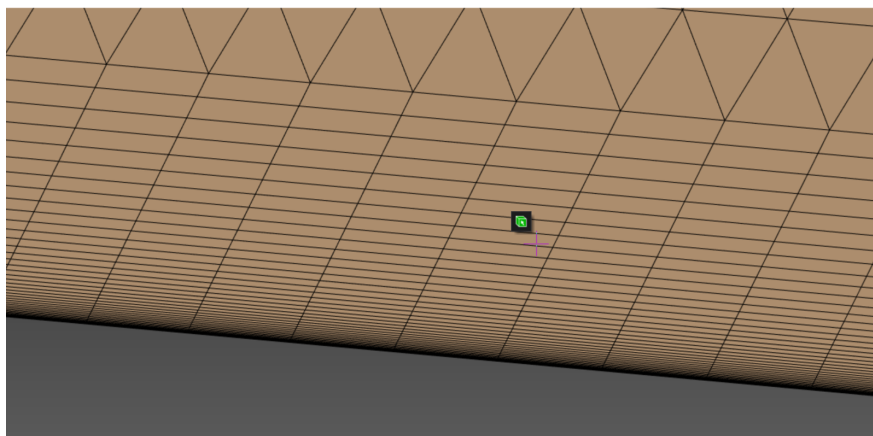
Figure 6.11. Inflation layers close up of a LES mesh

The mesh characteristics varied across the models, with uRANS requiring the least refinement and LES necessitating the highest resolution. All meshes were subjected to rigorous quality checks to ensure smooth transitions, minimal skewness, low orthogonality, and appropriate aspect ratios, critical for numerical stability.

6.2.1. Mesh and Grid Refinement

The computational domain was discretized with unstructured meshes refined in critical areas based on turbulence length scales and physical constraints. Detailed mesh configurations are presented in Table:

Parameter	uRANS	DES	LES
Number of Cells	278118	1695596	6029857
Boundary Layer Layers	13	33	40
First Cell Height (Δy_1)	$5 \times 10^{-6}\,\text{m}$	$5 \times 10^{-6}\,\text{m}$	$4 \times 10^{-6}\,\text{m}$
Cell Size in Wake (Δx)	$0.1\,\text{m}$	$2.5 \times 10^{-2}\,\text{m}$	$9.51 \times 10^{-3}\,\text{m}$
Growth Rate	1.2	1.2	1.1

Table 6.1. Comparison of mesh characteristics for uRANS, DES, and LES simulations.

This comparative approach ensured that each turbulence model was supported by a mesh tailored to its unique requirements, balancing resolution, accuracy, and computational cost.

6.3. Flow Conditions

The flow conditions were carefully selected to reflect realistic aerodynamic scenarios while maintaining consistency across all turbulence models. These parameters, including angle of attack, Mach number, and Reynolds number, were chosen to investigate the aerodynamic behavior of the NACA 2412 airfoil under challenging but practical conditions.

6.3.1. Mach Number and Atmospheric Conditions

The freestream Mach number was set to $M = 0.3$, corresponding to low subsonic flow. This choice ensures incompressible flow assumptions remain valid while allowing the exploration of flows where significant flow separation and turbulence can occur. The simulations were conducted under standard atmospheric conditions at sea level:

- Temperature: $T = 293.15$ K.
- Pressure: $p = 101325$ Pa.

These conditions establish a reference dynamic viscosity and density, which are essential for calculating the Reynolds number and simulating realistic fluid dynamics.

6.3.2. Reynolds Number

The Reynolds number for the simulations was determined based on the airfoil's chord length of 1 m, the freestream velocity derived from the Mach number, and the standard

atmospheric conditions. The resulting Reynolds number is sufficiently high to ensure turbulent flow over the airfoil, making it a relevant test case for validating the performance of the turbulence models.

At a temperature of 293.15 K and a pressure of 101,325 Pa, the speed of sound was calculated as $a = 343.2\,\text{m/s}$, yielding a freestream velocity of $V = 102.96\,\text{m/s}$. The Reynolds number, based on the chord length of 1 m, was calculated as:

$$\text{Re} = \frac{\rho V L}{\mu} \approx 6.85 \times 10^6,$$

where the air density (ρ) was determined using the ideal gas law, and the dynamic viscosity (μ) was assumed to be $1.81 \times 10^{-5}\,\text{Pa·s}$.

6.3.3. Turbulence Intensity and Length Scale

The turbulence intensity at the inlet boundary was set to 10%, which is representative of moderate turbulence levels typically found in industrial applications and ensures a robust transition to turbulence in the boundary layer. The turbulence length scale was specified as 0.4 times the thickness of the first boundary layer cell, following best practices outlined in the ANSYS manual for the SST k-ω model. This ensures that the turbulence characteristics are resolved accurately near the wall, capturing the effects of near-wall dynamics. For consistency, the same turbulence intensity and length scale were applied to all turbulence models, even though the resolution and modeling requirements differ between approaches.

6.3.4. Angle of Attack

An angle of attack (AoA) of 30° was chosen to simulate a high-lift condition where flow separation is prominent. This AoA is beyond the linear aerodynamic regime and represents a challenging test case for turbulence models, particularly in capturing separation dynamics, unsteady flow behavior, and wake development. This condition is of critical importance in applications such as stalled wing aerodynamics, where accurate prediction of flow separation and reattachment is essential for performance and safety assessments.

6.3.5. Summary of Flow Parameters

The chosen flow parameters are summarized in the table:

Parameter	Value
Mach Number	0.3
Temperature (T)	293.15 K
Pressure (p)	101325 Pa
Reynolds Number	Based on 1 m chord
Turbulence Intensity	10%
Turbulence Length Scale	$0.4\delta_1$ (first boundary layer thickness)
Angle of Attack (AoA)	30°

Table 6.2. Summary of Flow Conditions for Simulations

6.4. Solver Type

A density-based solver was used for all simulations due to its robustness in compressible flow cases. The solver efficiently handles transient flows and was configured for implicit time integration to ensure numerical stability across a range of time-step sizes. For LES and DES, where unsteady effects dominate, a transient simulation framework was employed.

6.5. Time Step Size

The selection of time-step sizes (Δt) was critical to resolve the temporal dynamics of the flow structures accurately while ensuring numerical stability. The process of determining appropriate time-step sizes involved several assumptions and simplifications based on the flow physics and computational constraints.

First, the CFL condition was employed as a primary guideline to ensure stability. For transient simulations, the CFL number was required to remain below unity in critical flow regions, particularly near the airfoil surface and in the wake. The CFL number is defined as:

$$\text{CFL} = \frac{U\Delta t}{\Delta x}, \tag{8}$$

where U is the characteristic velocity, Δt is the time-step size, and Δx is the cell size.

For LES and DES, the time-step sizes were constrained by the characteristic time scales of turbulence to capture both the large energy-containing eddies and the interaction of smaller scales. The large eddy turnover time, defined as $T_{eddy} = L/U$, where L is the integral length scale and U is the characteristic velocity, was used as a reference to ensure the time-step size aligned with the dominant unsteady flow dynamics.

Additionally, the Taylor microscale, which represents an intermediate turbulence scale where viscous and inertial effects interact, was used to validate the mesh and temporal resolution. The Taylor microscale was estimated using:

$$\lambda_{\text{Taylor}} = \left(\frac{15\nu u'^2}{\epsilon}\right)^{1/2}, \tag{9}$$

where ν is the kinematic viscosity, u' is the root mean square of velocity fluctuations, and ϵ is the turbulence dissipation rate. For the current setup:

- For LES: $u' \approx 10.5\,\text{m/s}$, $\epsilon \approx 12.34\,\text{m}^2/\text{s}^3$, and $\nu = 1.46 \times 10^{-5}\,\text{m}^2/\text{s}$, yielding $\lambda_{\text{Taylor}} \approx 0.237\,\text{m}$.
- For DES: Using similar parameters but with a coarser grid resolution, $\lambda_{\text{Taylor}} \approx 0.315\,\text{m}$.

The selected time-step sizes and corresponding CFL numbers were:

- **LES:** $\Delta t = 0.001\,\text{s}$, corresponding to approximately $T_{eddy}/10$, where $T_{eddy} \approx 0.0095\,\text{s}$. This resolution ensures the accurate capture of energy-containing eddies. The CFL number was approximately 3.15 due to time limitations. For proper approach CFL=1 should be considered.
- **DES:** $\Delta t = 0.001\,\text{s}$, determined using a similar approach as LES. While the CFL number in critical regions was approximately 1.2, the DES framework accommodates this by dynamically transitioning between RANS-like behavior near the wall and LES in separated regions.
- **uRANS:** $\Delta t = 0.002\,\text{s}$, ensuring a CFL number of approximately 0.6 in critical flow regions, sufficient for resolving time-averaged turbulence effects.

This methodology provided a balance between temporal accuracy and computational efficiency, ensuring the key flow dynamics were captured for LES and DES without excessive computational cost.

6.5.1. Temporal and Spatial Discretization Schemes

Temporal and spatial discretization schemes were kept as initial in the programe to ensure accuracy in resolving turbulent flow structures. Due to focus of this project on the turbulence models influence, not methods, one did not focus on that.

6.5.2. Convergence Criteria

The convergence criteria were defined to ensure reliable and accurate results:

- Residuals for all governing equations were monitored, with a convergence threshold of 10^{-3} for continuity, momentum and turbulence equations.
- For transient simulations, global quantities such as lift and drag coefficients were tracked until periodicity or steady behavior was observed.

7. Results and Discussion

This section presents the findings from the simulations, focusing on the key flow properties captured during the first 1s of the simulation. Due to computational constraints and the premature termination of the LES simulation, only vorticity contours are available for the LES case. The results include pressure and velocity contours, as well as vorticity distributions, providing insights into the flow dynamics for the completed simulations.

7.1. Pressure Contours

7.1.1. RANS

The pressure contour plots reveal a distinct low-pressure region near the leading edge which is as expected. This low-pressure area is indicative of high local suction, contributing to aerodynamic lift. The smooth pressure gradients across the domain highlight the absence of shock waves or abrupt pressure changes, aligning with the steady-state nature of the RANS simulation.
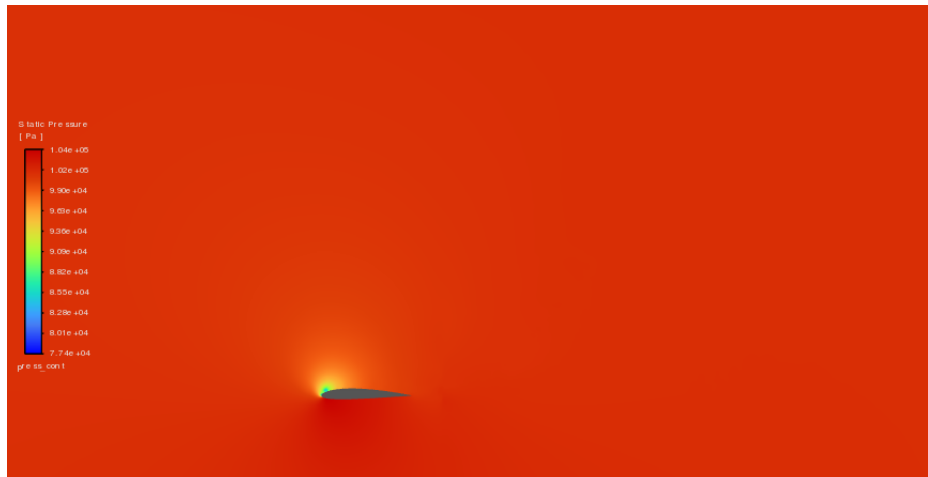
Figure 7.1. RANS pressure contours

7.1.2. uRANS

During the URANS turbulence model simulation, small disturbances in the pressure field were observed (7.2), leading to localized areas of reduced pressure. These regions corresponded to increased velocity, potentially giving rise to small vortices (7.3). Over the course of the simulation, extending to nearly 1s, the flow showed a tendency to stabilize, resembling the steady-state behavior of the RANS model (7.4). This stabilization highlighted the absence of strong, persistent vortices, with the flow aligning closely to the mean flow patterns typical of RANS simulations. Point of greatest pressure can be noticed, where one expect stagnation to occur.

26
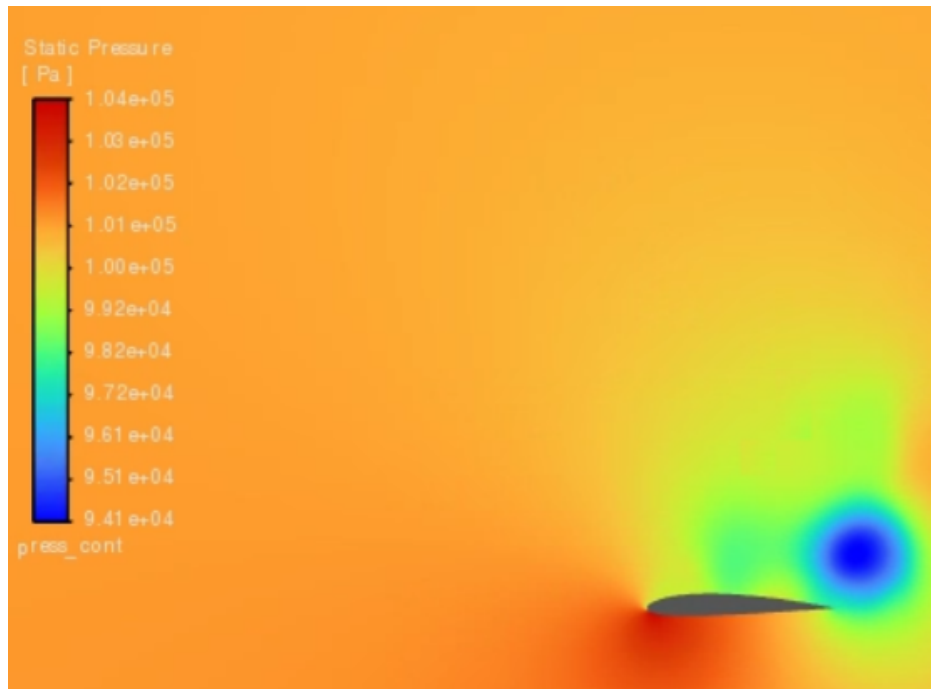
Figure 7.2. uRANS pressure contours $\Delta t = 0.281s$
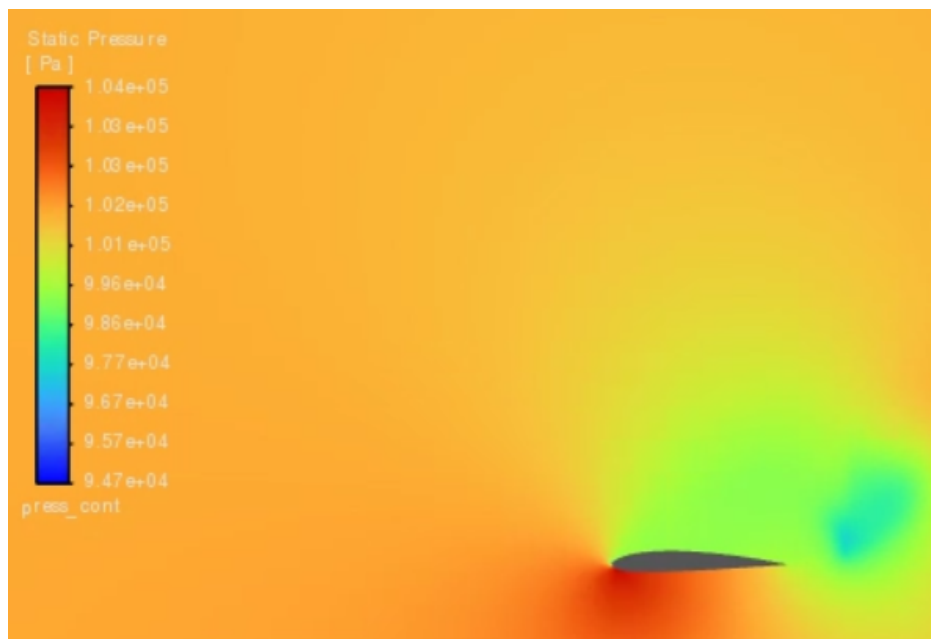
Figure 7.3. uRANS pressure contours $\Delta t = 0.781s$
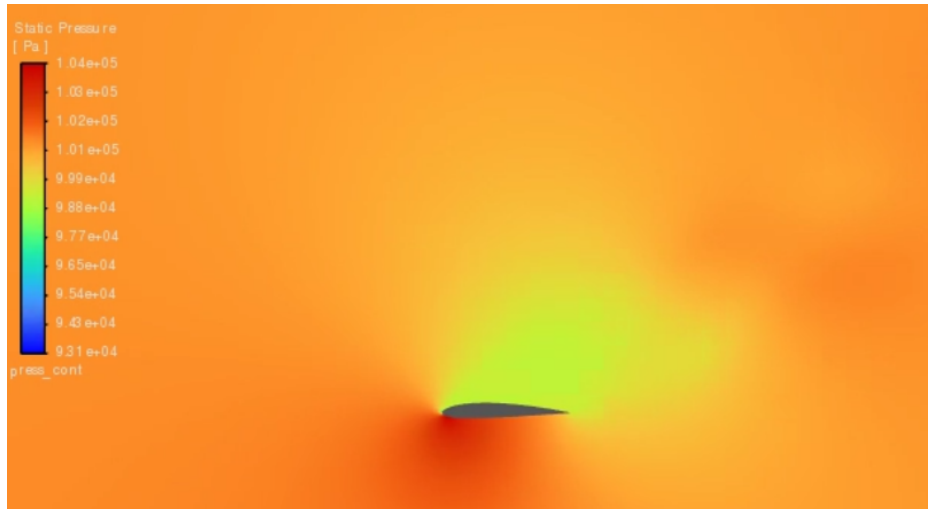
Figure 7.4. uRANS pressure contours $\Delta t = 0.840 s$

7.1.3. DES

The pressure contours obtained from the DES simulation offer insight into the significant pressure gradients that drive flow dynamics. These gradients play a crucial role in vortex formation and flow separation. Early in the simulation (7.5), areas of lower pressure begin to emerge, aligning with the initiation of vortices. As the flow develops (7.6), the pressure contours reveal regions where the fully developed vortices cause pronounced fluctuations, particularly in the wake. Toward stabilization (7.7), the contours show developing large-scale structures, reflecting the hybrid approach of DES in resolving both steady RANS-like near-wall regions and unsteady LES-like wake regions.
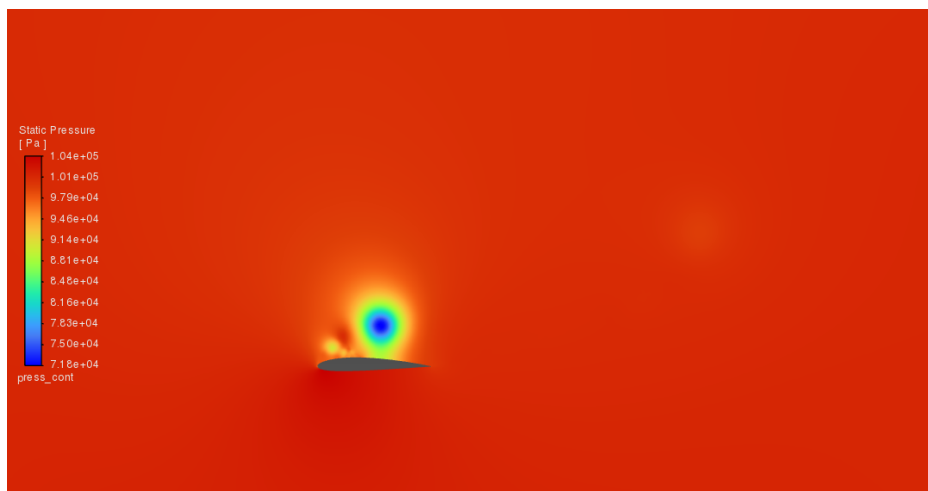
Figure 7.5. DES pressure contours $\Delta t = 0.045 s$
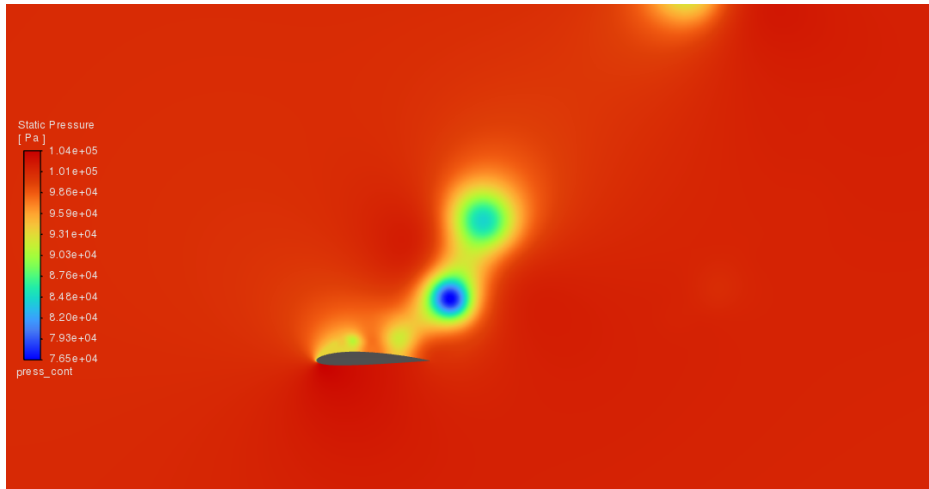
Figure 7.6. DES pressure contours $\Delta t = 0.461\,s$
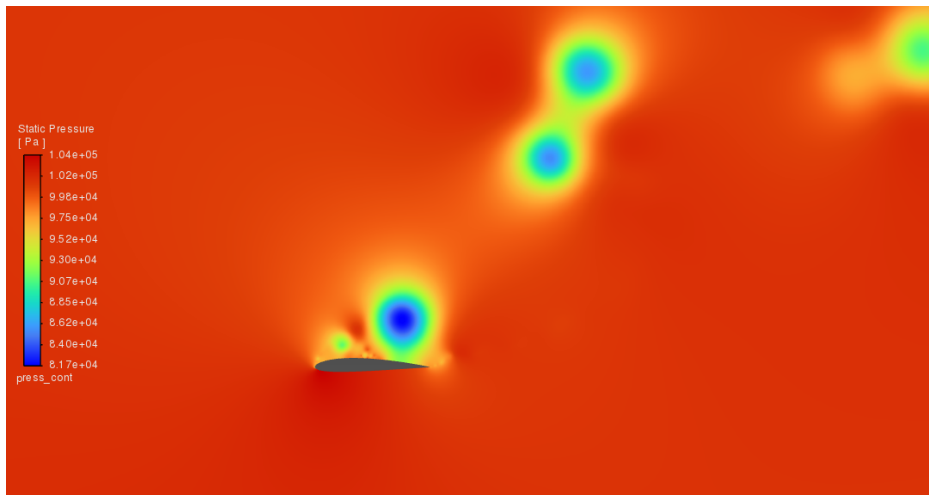
Figure 7.7. DES pressure contours $\Delta t = 0.999\,s$

7.2. Velocity Contours

7.2.1. RANS
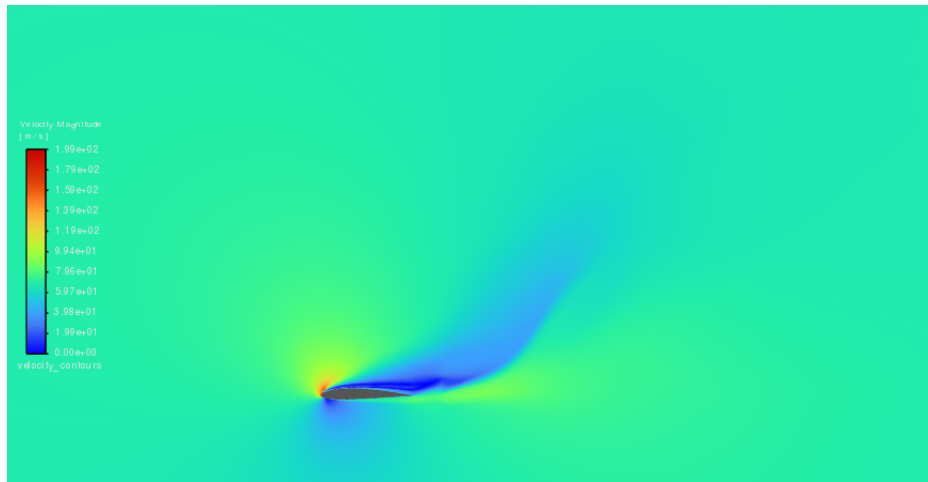
Figure 7.8. RANS velocity contours

The contour plot of vorticity from the RANS simulation does not reveal any prominent large-scale vortices. While some regions of vorticity are visible, they are relatively mild and lack the complexity typically associated with turbulent flow structures. The absence of pronounced vortices aligns with the steady-state nature of the RANS approach, which primarily captures the mean flow and suppresses transient or intricate vortex dynamics.

7.2.2. uRANS

The velocity contours display notable flow features that align with the 30° upward flow orientation. A distinct acceleration of the flow is observed along the lower surface, creating a high-velocity path due to the inclined geometry (7.10). This region of increased velocity corresponds to an area of reduced pressure, as expected from the pressure-velocity relationship. On the upper surface, the flow decelerates, forming a zone of lower velocity, which further accentuates the pressure difference across the domain. Additionally, the presence of vortices (7.9) can be inferred from the shear regions near the separation points, where the flow transitions between high and low velocity. Over the simulated time frame, the velocity field stabilizes (7.11), converging towards a steady-state profile reminiscent of the RANS model's predictions.
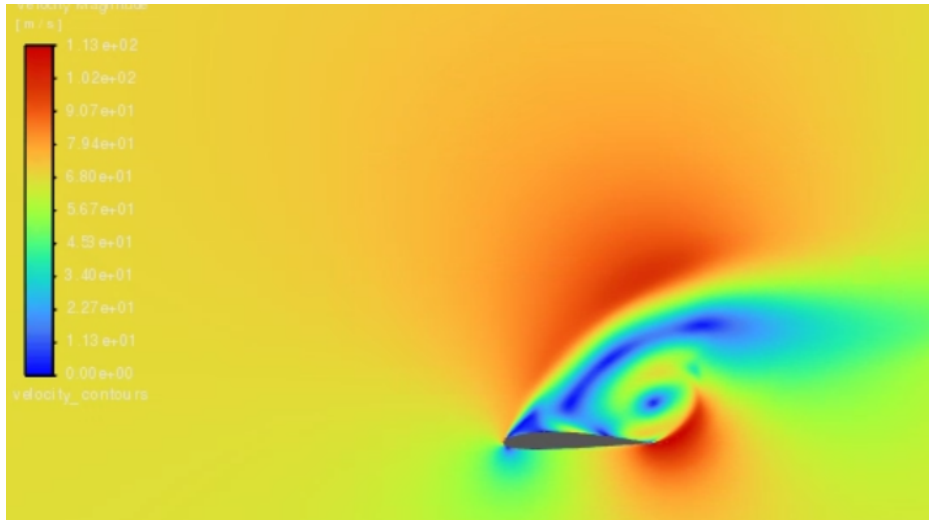
Figure 7.9. uRANS velocity contours $\Delta t = 0.212s$
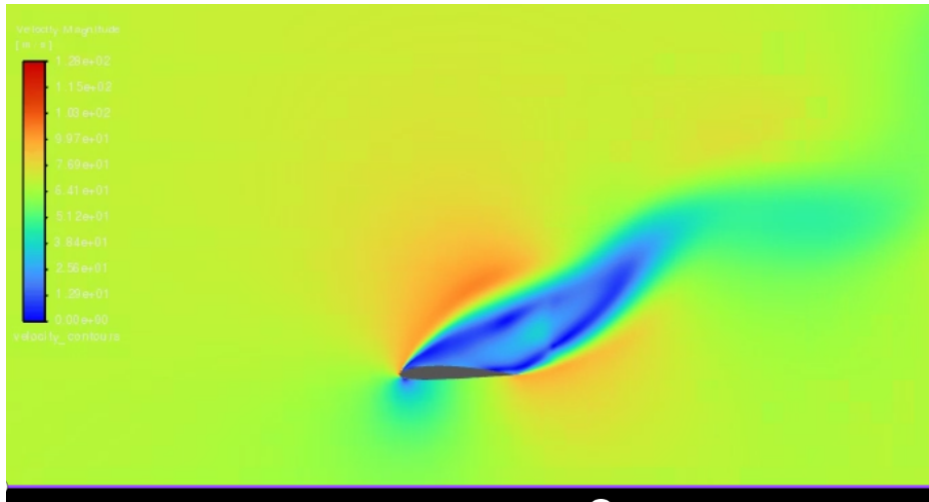
Figure 7.10. uRANS velocity contours $\Delta t = 0.469s$
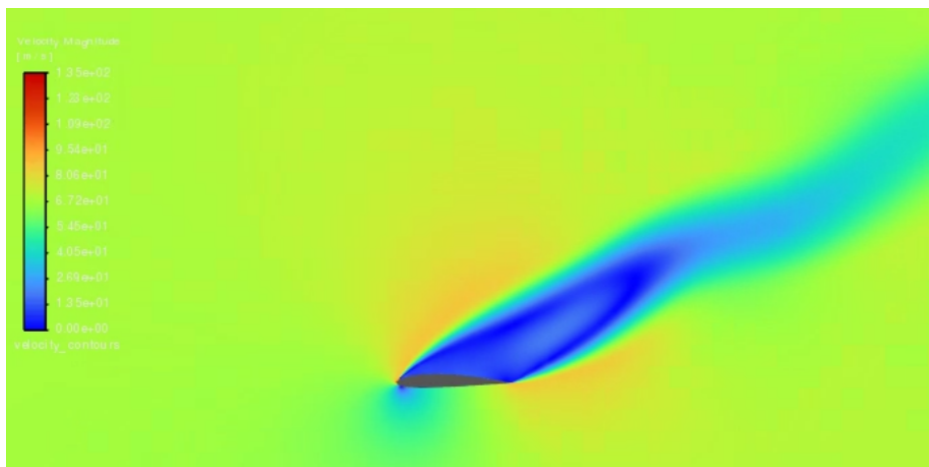
Figure 7.11. uRANS velocity contours $\Delta t = 0.925s$

7.2.3. DES

Velocity contours in the DES simulation illustrate the evolution of flow patterns through acceleration and deceleration regions. Early snapshots (7.12) show distinct high-velocity paths forming near areas of lower pressure, creating the shear layers that promote vortex generation. As vortices fully develop (7.13), velocity contours highlight their influence on the wake, showcasing swirling patterns and zones of intense shear. Even as the flow approaches stabilization (7.14), larger vortices persist, contrary to the near-uniform velocity field expected in traditional steady models. This demonstrates DES's capability to maintain unsteady features while capturing the transition to stabilized flow.
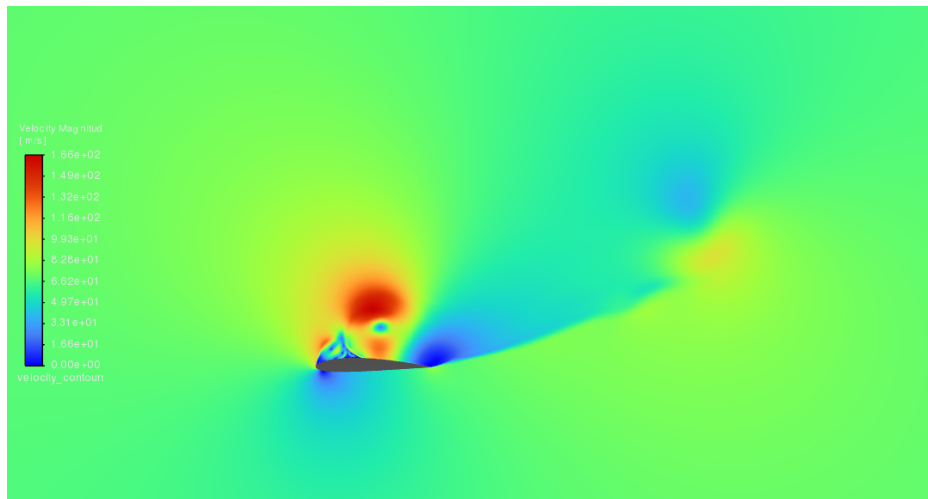
Figure 7.12. DES velocity contours $\Delta t = 0.045 s$
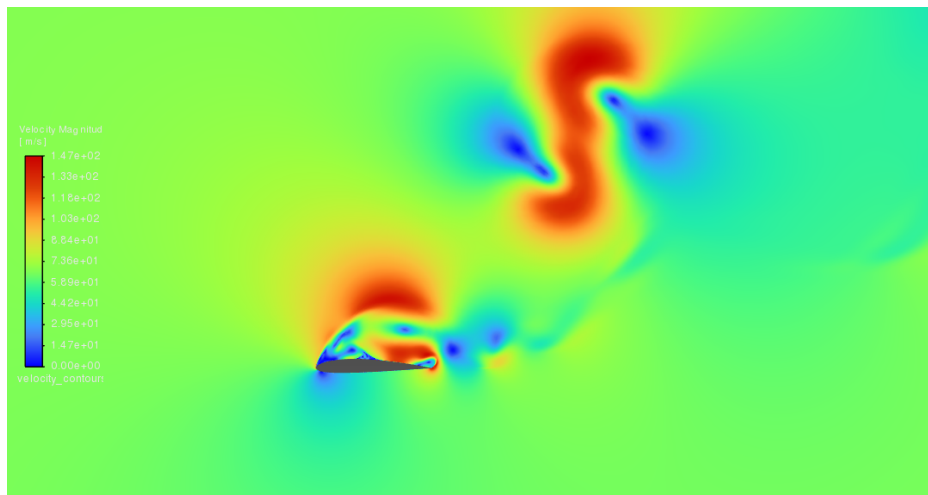
Figure 7.13. DES velocity contours $\Delta t = 0.424 s$
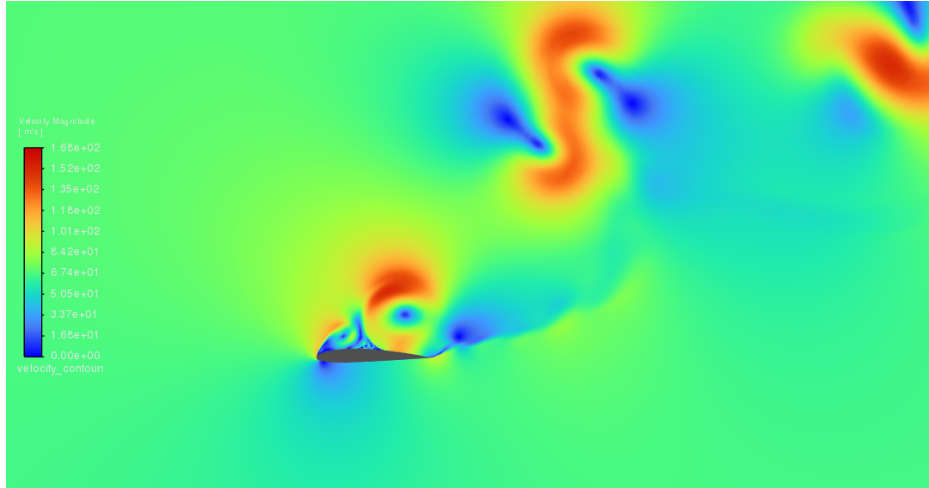
Figure 7.14. DES velocity contours $\Delta t = 0.999 s$

7.3. Vorticity Contours

7.3.1. RANS

In RANS simulations, vorticity contours show smooth, relatively featureless regions, reflecting the averaged nature of turbulence modeling. Unlike LES or DES, where large vortices are directly captured, RANS smooths out the transient fluctuations, resulting in minimal visible vorticity. The contours primarily highlight smaller-scale, less dynamic features, such as weak shear layers or regions near flow separation, but they do not capture the strong, large-scale vortices found in unsteady simulations 7.15).
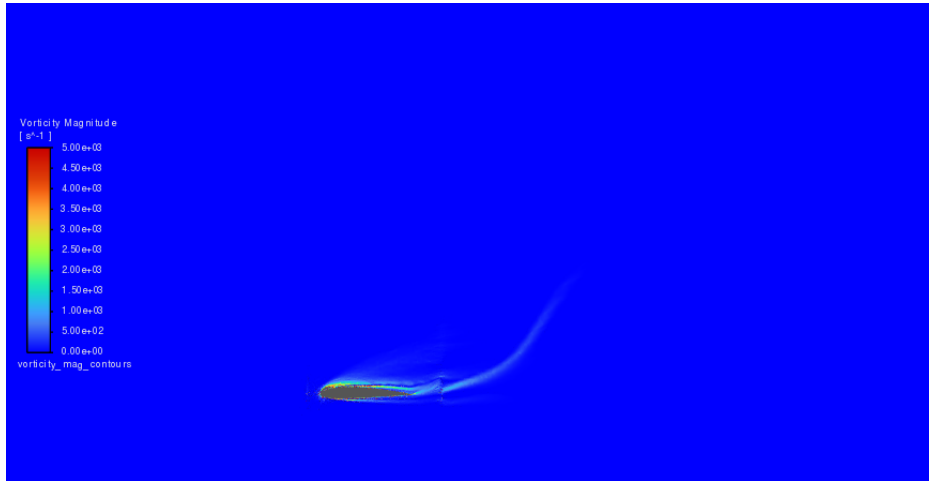
Figure 7.15. RANS vorticity contours

7.3.2. uRANS

The vorticity contours reveal the presence of structured vortices (7.16), particularly in regions where the flow undergoes acceleration or deceleration. These vortices are most prominent near the trailing edge, where velocity gradients are steep. The rotational

structures are indicative of flow instabilities generated by shear and pressure gradients, but no large-scale unsteady vortices dominate the domain (7.17). As the simulation progresses, the vorticity field stabilizes, mirroring the characteristics of a steady flow regime with not highly visible rotational zones (7.18). This stabilization suggests a convergence of the flow towards a quasi-steady state, aligning with the observations from the velocity contours.
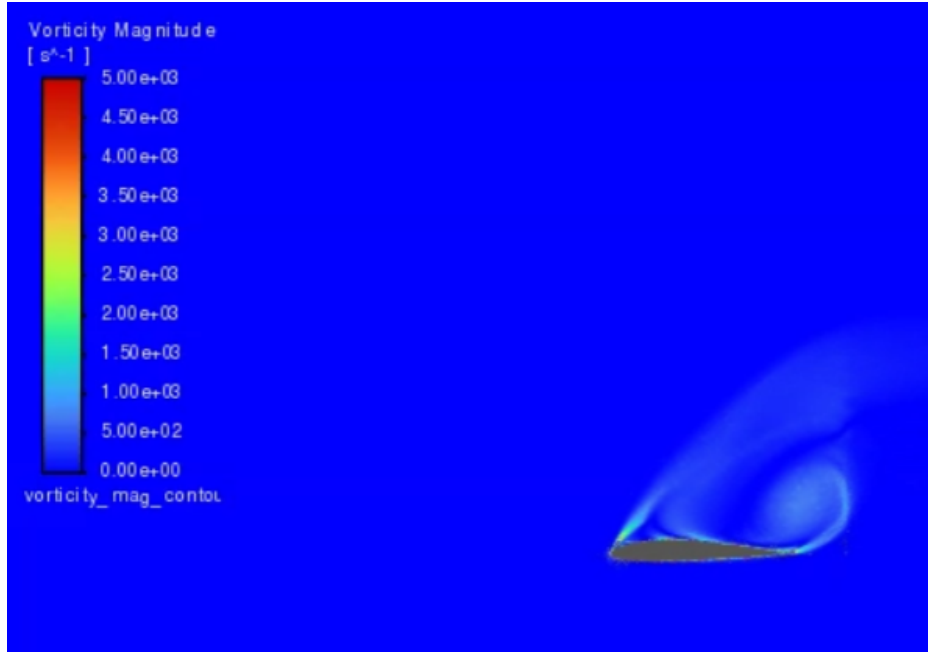
Figure 7.16. uRANS vorticity contours $\Delta t = 0.086s$
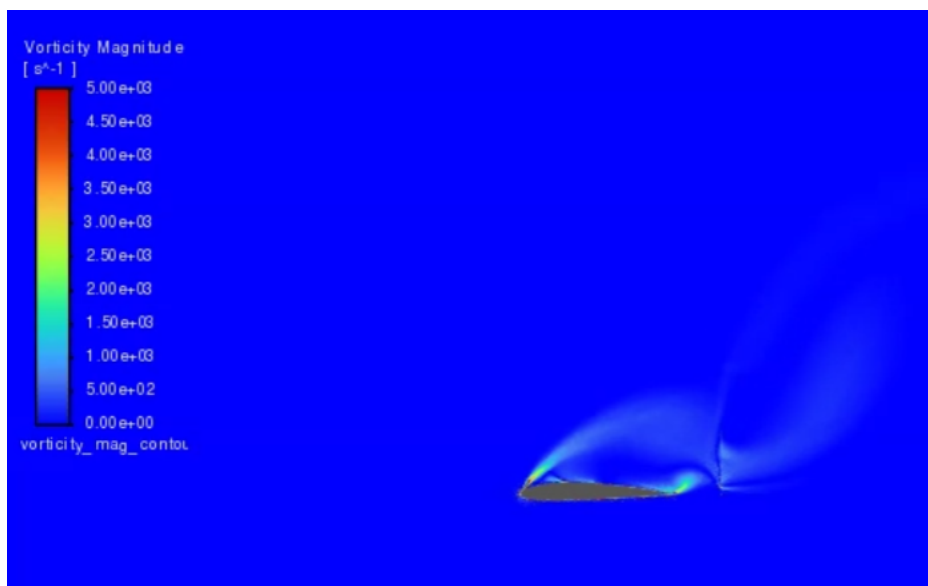
Figure 7.17. uRANS vorticity contours $\Delta t = 0.426s$
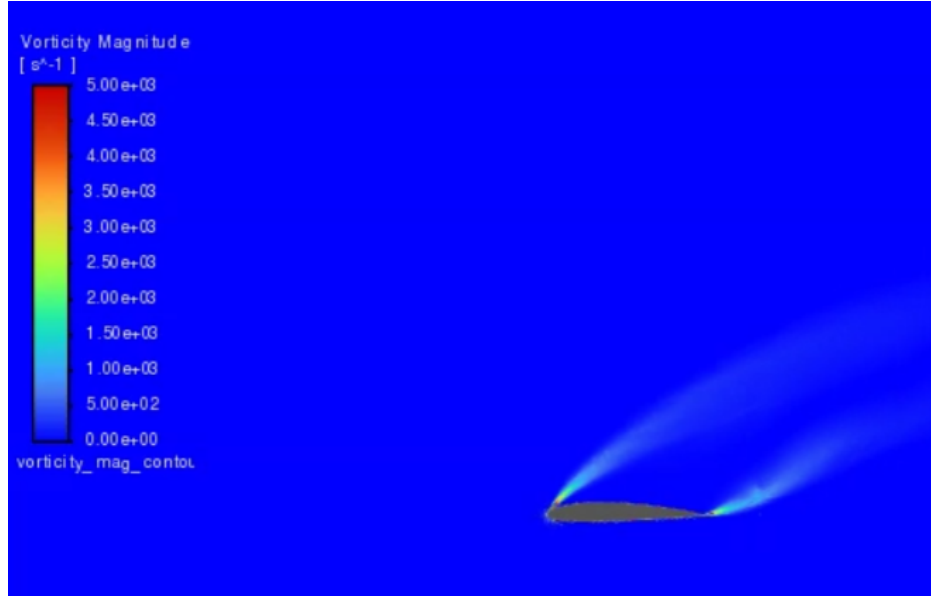
Figure 7.18. uRANS vorticity contours $\Delta t = 0.831 s$

7.3.3. DES

Vorticity contours provide a comprehensive view of rotational flow structures and turbulent energy distribution in the DES simulation. Initial contours capture the onset of small rotational regions in areas of pressure and velocity gradients (7.20, 7.19), marking the beginning of vortex formation. As the flow progresses, fully developed vortices dominate the wake (7.22, 7.21), showcasing DES's ability to resolve unsteady and large-scale rotational features. In the later stages, despite the overall flow stabilization, the vorticity contours reveal significant lingering vortices(7.26,7.24). These structures underscore the hybrid DES model's effectiveness in preserving turbulent details across different regions of the domain, making it a vital tool for studying complex aerodynamic flows.
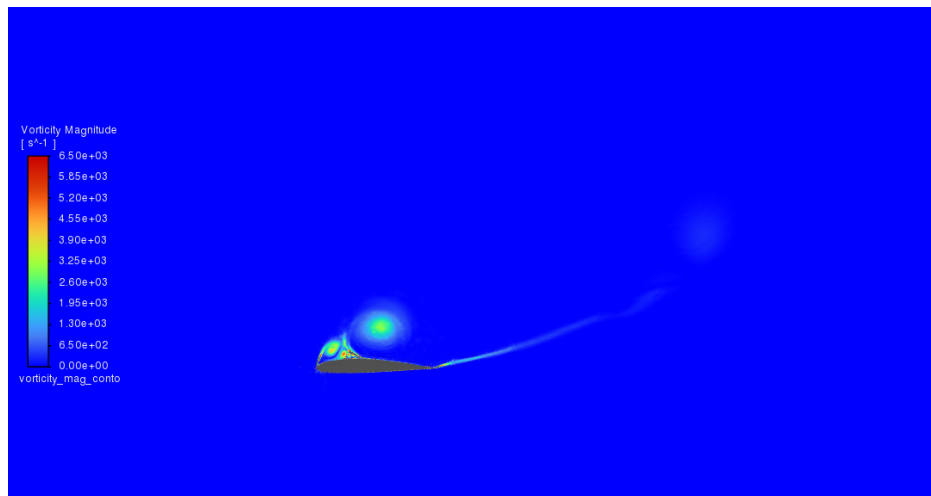
Figure 7.19. DES vorticity contours $\Delta t = 0.045 s$
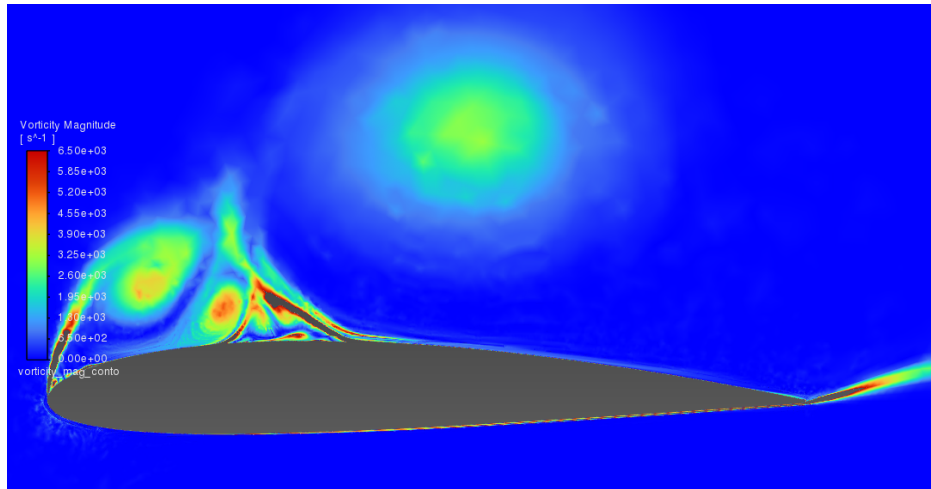
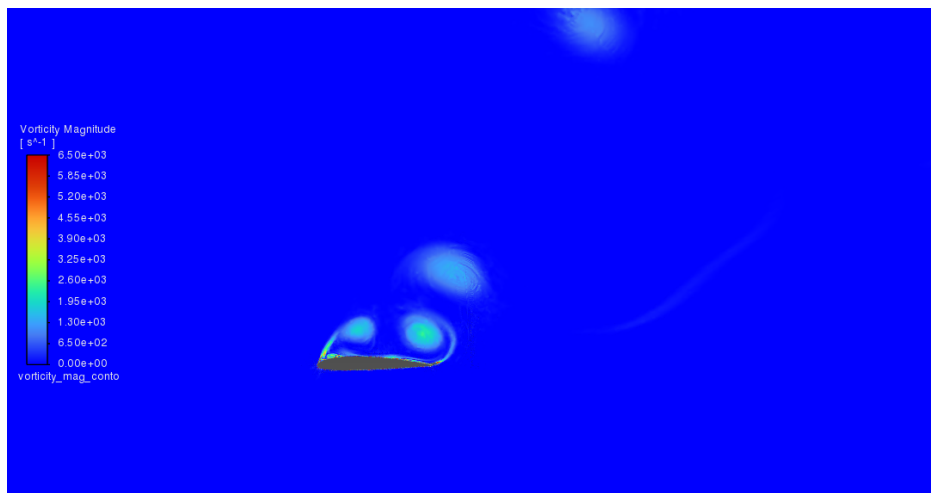**Figure 7.20.** DES vorticity contours close-up $\Delta t = 0.045s$

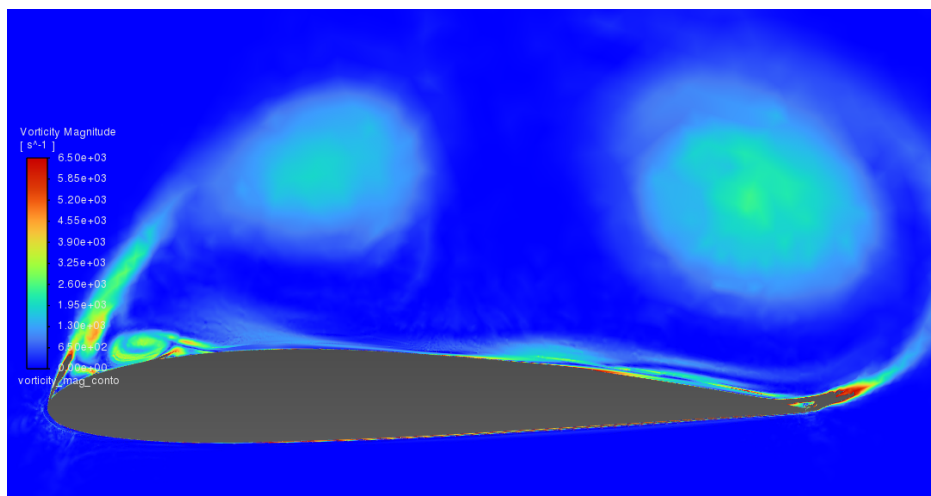

Figure 7.21. DES vorticity contours $\Delta t = 0.381s$

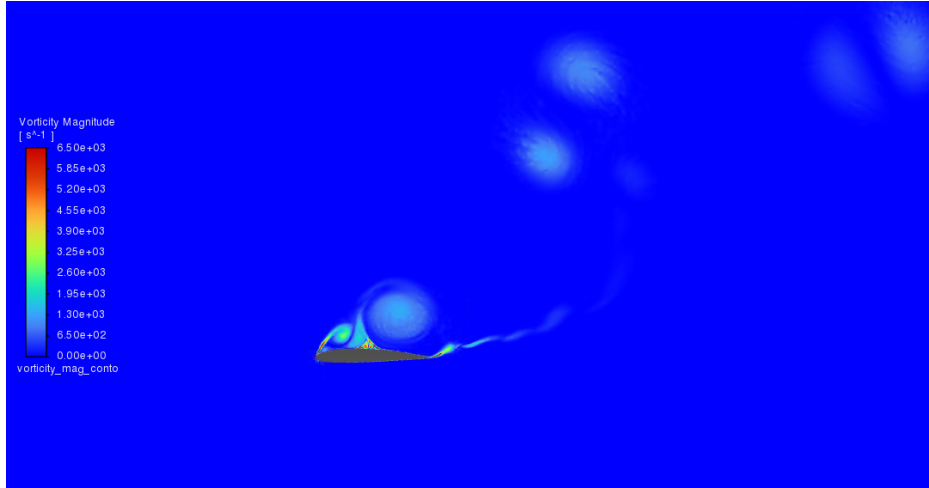**Figure 7.22.** DES vorticity contours close-up $\Delta t = 0.381s$

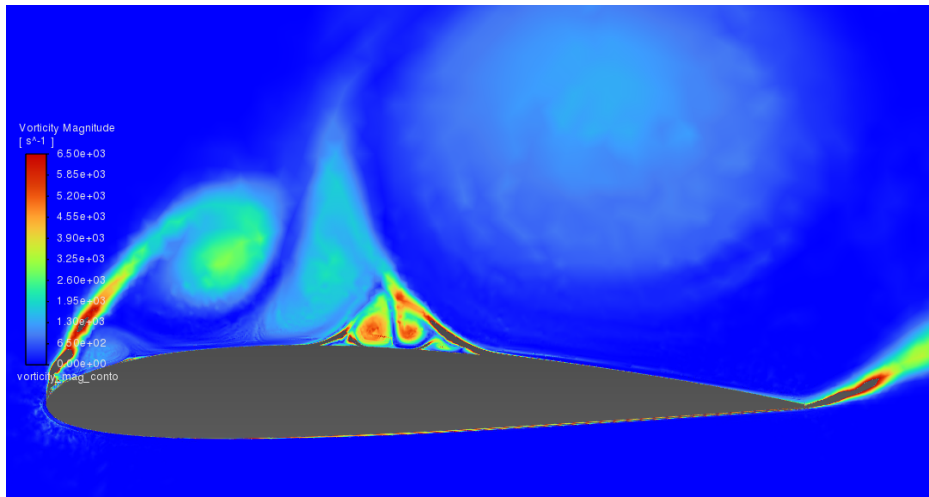**Figure 7.23.** DES vorticity contours $\Delta t = 0.998\,s$

Figure 7.24. DES vorticity contours close-up $\Delta t = 0.998\,s$

7.3.4. LES

In the context of vorticity contours for the airfoil simulation, the LES model highlights the formation, development, and dynamics of vortices throughout the flow domain.

Initially at the onset of the simulation, the LES model resolves the formation of small vortices due to the interaction of the boundary layer with the freestream. These vortices initially appear as weak, scattered rotational features near the leading edge of the airfoil and along the upper surface, where velocity gradients are steep. As flow disturbances trigger vortex shedding, the initial vorticity contours reveal small-scale rotational structures that will eventually grow into larger, more defined vortices.
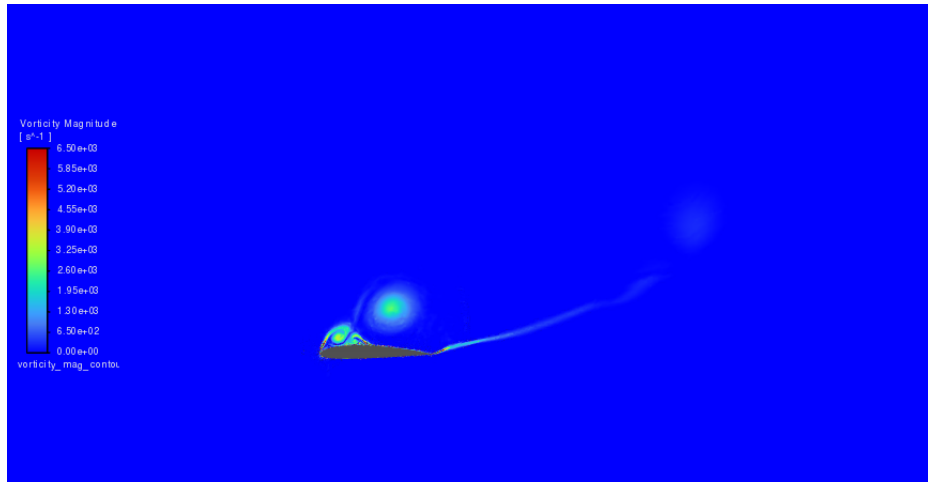
37

Figure 7.25. LES vorticity contours $\Delta t = 0.045 s$

As the simulation progresses, these nascent vortices grow and merge, evolving into more coherent and organized structures. The vorticity contours in this phase show the formation of large-scale vortices in the wake, as well as in the separated regions, especially on the lower surface of the airfoil. These vortices are fully developed and exhibit a high intensity in the contour plots, indicating their significant role in the energy transfer and turbulent mixing within the flow. The LES model captures the unsteady nature of these structures, revealing their time-varying characteristics, such as vortex shedding and the intermittent behavior of the vortices.
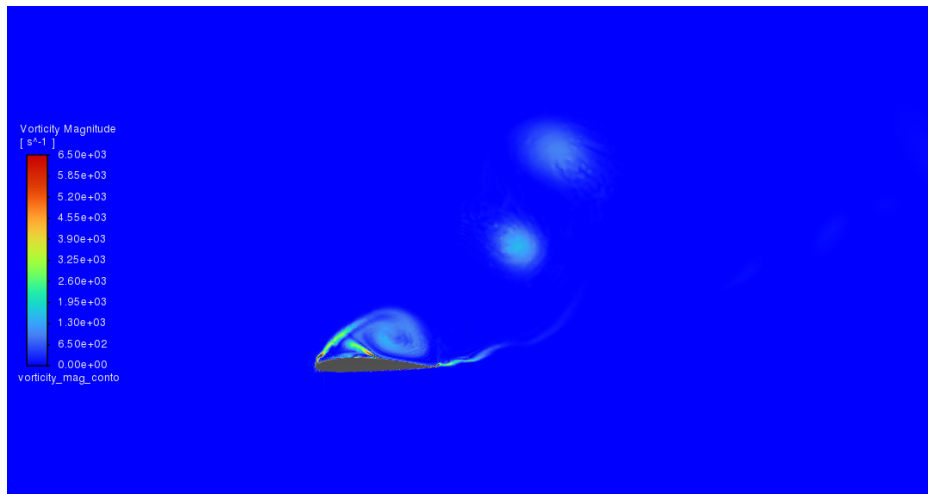

Figure 7.26. LES vorticity contours $\Delta t = 0.381 s$

Toward the end of the simulation, while the flow as a whole stabilizes, significant vorticity remains in the wake. The contours still display pronounced vortices, particularly in the wake region behind the airfoil, indicating that the LES model retains the ability to resolve the turbulence dynamics even in the quasi-steady state. Unlike RANS or uRANS, where the turbulence is averaged out, the LES model continues to capture the persistent,

unsteady features of the vortex structures, which is a key advantage of the approach. These lingering vortices, although smaller than in the earlier stages, are still large compared to what might be seen in traditional steady-state simulations, underlining LES's capability to capture the dynamic nature of turbulence.
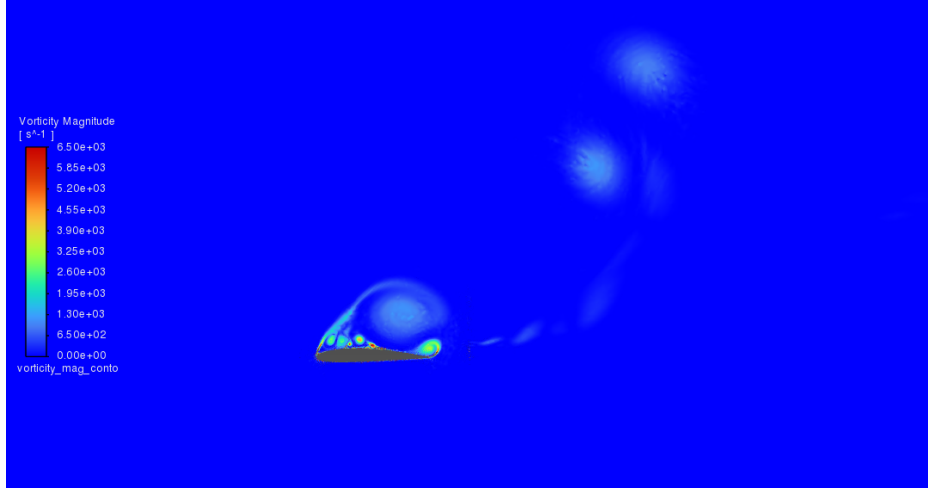

Figure 7.27. LES vorticity contours $\Delta t = 0.938s$

7.4. Comparative Analysis

In this study, we evaluated three turbulence models: uRANS, DES, and LES—by analyzing their performance in simulating the flow dynamics over an aerodynamic airfoil. Through a comprehensive comparison, we gained valuable insights into each model's strengths, weaknesses, and computational cost versus accuracy trade-offs. The results highlighted the distinct capabilities of each model in capturing turbulent flow features, vortex dynamics, and flow separation, allowing for a deeper understanding of their suitability for different aerodynamic scenarios.

7.4.1. Strengths and Weaknesses of the Models

The analysis demonstrated that **uRANS** is the most computationally efficient model, making it ideal for steady-state simulations or cases where a simplified representation of turbulence is sufficient. However, while uRANS provided reasonable predictions for overall flow trends, it was unable to capture unsteady flow features like vortex shedding and wake turbulence, which are essential for understanding the performance of aerodynamic surfaces in more dynamic conditions.

DES presented a balanced approach, combining the efficiency of RANS in near-wall regions with the accuracy of LES in the more dynamic regions. This hybrid model proved effective in resolving large-scale unsteady features like vortex shedding and flow separation. However, DES still had limitations, particularly in fully resolving turbulence in the near-wall regions, where it continued to rely on RANS formulations. Despite this, DES

provided a good balance between computational cost and turbulence resolution, making it suitable for flows with moderate unsteadiness.

LES was the most accurate in capturing the full spectrum of turbulence structures, especially in the wake and separated flow regions. Its ability to directly resolve large eddies and time-varying turbulence allowed for an in-depth understanding of vortex dynamics. However, this high level of accuracy came with a substantial computational cost, particularly in fine grid resolution near the wall, making LES the most resource-intensive model.

7.4.2. Computational Cost Versus Accuracy Trade-offs

The comparative analysis revealed clear trade-offs between computational cost and accuracy. **uRANS** emerged as the most computationally efficient model, suitable for steady or moderately unsteady flows where detailed turbulence resolution was not necessary. It allowed for quick simulations, making it ideal for preliminary studies but at the cost of limited accuracy in dynamic flow scenarios.

DES provided a reasonable compromise, offering better accuracy in resolving unsteady features than uRANS but still relying on RANS in the near-wall regions, which resulted in higher computational costs compared to uRANS. DES was suitable for flows with moderate unsteadiness, where a balance between computational efficiency and the need for accurate turbulence resolution was essential.

LES, while offering the highest accuracy by resolving turbulence at a much finer scale, incurred the greatest computational expense. The detailed resolution required for LES, particularly near-wall, made it the most resource-demanding model. Despite this, its ability to capture the full range of turbulent features, especially in highly dynamic flow conditions, made LES the preferred choice for simulations where precision in transient flow behavior was critical.

7.4.3. Model Performance

Key insights from the study emphasized that **uRANS** is well-suited for scenarios where flow dynamics are relatively steady, or where approximate turbulence representations are acceptable. However, it is less effective in capturing unsteady phenomena, such as vortex shedding, which limits its applicability in more complex aerodynamic analyses.

DES, with its hybrid approach, offered significant improvements in capturing unsteady turbulence features, particularly in the wake and separation zones. Its performance in balancing computational cost and accuracy made it suitable for practical applications where moderate unsteadiness is expected. However, it still faced challenges in fully resolving turbulence in the near-wall regions due to the reliance on RANS formulations.

LES stood out as the most accurate model for resolving large eddies, vortex dynamics, and time-varying turbulence. It proved invaluable for studying complex aerodynamic flows with high unsteadiness. However, the computational cost required for LES simula-

tions makes it most suitable for applications where the detailed resolution of turbulent features is essential, and where sufficient computational resources are available.

7.4.4. Future Work

While this study has provided meaningful insights into the performance of the turbulence models, several directions for future work remain:

Enhanced Model Validation: To further improve the reliability and applicability of the turbulence models, future research could focus on validating the simulation results against experimental data or more complex benchmark cases, particularly in cases involving highly unsteady or transitional flows.

Higher Fidelity Grid Resolution: Increasing grid resolution, particularly in LES simulations, especially near-wall regions, would improve the accuracy of the turbulence representation, allowing for better predictions of boundary layer dynamics and flow separation.

Development of Advanced Hybrid Models: Exploring advanced hybrid models that could dynamically transition between RANS and LES regions based on flow characteristics would enhance both the accuracy and efficiency of turbulence simulations. These models could focus on resolving critical turbulence features while optimizing computational effort.

Machine Learning for Turbulence Modeling: Integrating machine learning techniques to optimize turbulence models could improve simulation efficiency. Machine learning could be used to identify the best model configurations, dynamic grid refinements, and adaptive strategies that improve model performance without significantly increasing computational cost.

Exploring Additional Flow Regimes: Extending the current study to cover more complex flow configurations, such as compressible flows or high-speed aerodynamic conditions, could provide further insights into the behavior of these turbulence models under varying flow regimes.

7.4.5. Project Summary and Contributions

This project provided a thorough analysis of the uRANS, DES, and LES models by comparing their ability to simulate turbulent flow over an airfoil. By analyzing key flow features such as pressure, velocity, and vorticity contours, we were able to assess each model's effectiveness in capturing unsteady phenomena like vortex shedding and wake dynamics.

- A detailed comparative analysis of the strengths and weaknesses of uRANS, DES, and LES.
- Insights into the computational trade-offs between accuracy and cost for each model, and recommendations for selecting the appropriate model based on the flow characteristics.

- A clear understanding of how DES balances the advantages of RANS and LES, providing improved performance for flows with moderate unsteadiness.
- Identification of potential improvements and areas for further research, particularly in the development of advanced hybrid models and machine learning-based optimization techniques.
- This work has practical implications for industries such as aerospace, automotive, and energy, where accurate predictions of turbulent flows are critical for optimizing design and performance.
- The results provide a foundation for further exploration of turbulence modeling techniques, offering valuable tools for engineers and researchers working to simulate and analyze complex aerodynamic flows.

Key contributions include:

8. Conclusion and Future Work

Summarize the key findings and implications:

- Recap of the turbulence models' performance.
- Potential applications of the results in engineering.
- Suggestions for future research directions (e.g., multiple angles of attack, higher Reynolds numbers, or experimental validation).

References

[1] A. John, *Fundamentals of Aerodynamics, 6th Edition.* 2017.

[2] P. Liu, *Aerodynamics.* 2021.

[3] Warsaw University of Technology, Faculty of Power and Aeronautical Engineering. "Lectures on fluid mechanics i: Lecture 15 ntroduction to hydrodynamic instability and turbulence". [Online; accessed 17 December, 2023]. (2016).

List of Figures

List of Tables

List of Appendices